Journal of Microscopy

Journal of Microscopy, Vol. 259, Issue 1 2015, pp. 26–35
Received 24 October 2014; accepted 17 February 2015

doi: 10.1111/jmi.12245

Dimensional metrology of lab-on-a-chip internal structures: a comparison of optical coherence tomography with confocal fluorescence microscopy

D.R. REYES*, M. HALTER† & J. HWANG‡

**Physical Measurement Laboratory, National Institute of Standards and Technology, Gaithersburg, Maryland, U.S.A.*
†Material Measurement Laboratory, National Institute of Standards and Technology, Gaithersburg, Maryland, U.S.A.
‡Physical Measurement Laboratory, National Institute of Standards and Technology, Boulder, Colorado, U.S.A.

Key words. Critical dimensions, dimensional metrology, ImageJ, laser-scanning confocal microscopy, optical coherence tomography, quantitative imaging.

Summary

The characterization of internal structures in a polymeric microfluidic device, especially of a final product, will require a different set of optical metrology tools than those traditionally used for microelectronic devices. We demonstrate that optical coherence tomography (OCT) imaging is a promising technique to characterize the internal structures of poly(methyl methacrylate) devices where the subsurface structures often cannot be imaged by conventional wide field optical microscopy. The structural details of channels in the devices were imaged with OCT and analyzed with an in-house written ImageJ macro in an effort to identify the structural details of the channel. The dimensional values obtained with OCT were compared with laser-scanning confocal microscopy images of channels filled with a fluorophore solution. Attempts were also made using confocal reflectance and interferometry microscopy to measure the channel dimensions, but artefacts present in the images precluded quantitative analysis. OCT provided the most accurate estimates for the channel height based on an analysis of optical micrographs obtained after destructively slicing the channel with a microtome. OCT may be a promising technique for the future of three-dimensional metrology of critical internal structures in lab-on-a-chip devices because scans can be performed rapidly and noninvasively prior to their use.

Introduction

Commercialization of lab-on-a-chip technologies is at a point where standardization has become a subject of increasing interest within the field. A number of possible parameters for standardization have made their appearance in the literature and roadmaps discussions at the international level. Among those parameters of interest are the microchannel's internal dimensions, the external device geometry, electroosmotic mobility and zeta potential, fluidic interfaces and autofluorescence (Becker, 2010; Stavis, 2012).

Depending on the material used, which is dictated by the application of interest, different parameters will become more or less important when defining which of them should be measured. Biological applications in lab-on-a-chip devices have exploded in recent years, and characteristic parameters of the materials most commonly used to carry out such applications represent important and likely candidates for standard testing. Historically, biological applications such as cell culture and molecular biology have made use of polymeric materials (e.g. polystyrene) in conventional consumable products, allowing for the disposal of such products after their usage. In the case of lab-on-a-chip devices, the field has used polymers such as polydimethylsiloxane, polymethylmethacrylate (PMMA) and polycarbonate, for a number of applications, including biological ones. Although the use of lab-on-a-chip devices in biological applications has greatly increased during the last decade, other applications also can benefit from polymeric materials as long as certain conditions, such as mild temperatures and water-based solvents, are met.

Being disposable is an attractive advantage that polymeric lab-on-a-chip devices offer since it eliminates a number of processes required for their reuse. For single-use devices, the reproducibility of critical features in final products will need to be assessed in order to assure batch-to-batch comparability. Fabrication parameters such as pressure and temperature could have negative unintended consequences in the dimensional properties of the final product. For example, whereas a master to be used in molding the polymeric material could have

Correspondence to: Darwin R. Reyes, Physical Measurement Laboratory, National Institute of Standards and Technology, 100 Bureau Drive, Gaithersburg, Maryland, U.S.A. Tel: +1-301-975-5466; fax: +1-301-975-5668; e-mail: darwin.reyes@nist.gov

the desired dimensions, the final product can have slightly different dimensions than expected. Alterations in the channel dimensions resulting from deviations in the fabrication process can affect the channel width and/or height. Small deviations of up to 2% can cause changes in the flow resistance up to 16% (Beebe *et al.*, 2002). These dimensional alterations can cause problems not only experimentally, but also when attempting to accurately model complex geometries. Therefore, methods to accurately measure internal microchannel dimensions would allow for manufacturers to define product specifications and foster improved device comparability and reliability, which could facilitate the commercialization of lab-on-a-chip technologies.

The characterization of internal structures in a polymeric device, especially for a final product, will require different measurement techniques than those traditionally used in the characterization of microelectronic devices. A number of well-known methods have been used to characterize structures within lab-on-a-chip devices. Some examples include scanning probe methods like atomic force microscopy (AFM), and optical techniques such as ellipsometry, confocal and interferometric microscopies. Those techniques can also be used to characterize lab-on-a-chip devices but have limited usefulness. The AFM provides a limited access to the corners of a device where flat surfaces intersect at a sharp angle, and its probe scans the exposed sample surface to allow for nanoscale evaluation. In addition, AFM characterization is limited to preassembled devices since final products will have channels that are inaccessible for such characterization. On the other hand, in optical imaging of the assembled devices, the resolution suffers due to an incoherent scattering signal at the sharp corners and a complex interference from multiple layers and surfaces. For instance, interferometry microscopy can produce three-dimensional images of internal structures (and has a field of view in the millimetre scale) as long as the top surface is completely transparent or the device has not been sealed with a lid. The above-mentioned optical techniques use light sources in the UV-Visible spectrum, which will produce more scattering than optical techniques that use wavelengths in the near-infrared region. Therefore, a new approach to characterize internal structures (e.g. microchannels) in lab-on-a-chip final product devices is essential for the development and possible future adoption of dimensional testing standards. However, no commercially available technique used for imaging lab-on-a-chip or microelectronic devices has all the required capabilities to image internal structures in lab-on-a-chip final products. Optical Coherence Tomography (OCT) is a technique that could provide the imaging capabilities required for the analysis of deep subsurface internal structures within completely sealed (final products) polymeric devices with poor optical transparency or thicknesses of up to a few millimetres (Choma *et al.* 2003; de Boer *et al.* 2003; Drexler and Fujimoto 2008; Frohman *et al.* 2008; Leitgeb *et al.* 2003). The use of OCT to examine microfluidic devices has been limited to qualitatively inspecting several bonding methods of polycarbonate and polydimethylsiloxane devices (Li *et al.*, 2011). Despite this initial demonstration, the OCT technique has not been broadly used in microfluidic applications mainly because promises and challenges of OCT in microfluidic devices have not been assessed. For instance, complex interference from multiple layers and surfaces may still arise due to autocorrelation artefacts in OCT, and these challenges need to be addressed to enable broad application of OCT techniques in characterizing microfluidic device structures. Delineation of these measurement challenges would advance the use of OCT for dynamic flow measurements with higher accuracy in microfluidic devices. Recent report on dynamic Doppler OCT (DOCT) on a millimetre scale tube demonstrated the potential expansion of the DOCT technology in characterizing dynamic flow patterns in microfluidic applications (Villey *et al.*, 2010).

In the work presented here, we developed an in-house written ImageJ Macro to analyze the OCT and laser-scanning confocal microscopy (LSCM) images collected from a PMMA lab-on-a-chip device. The device in its final form is expected to have four channels of the same dimensions (height and width) on the master template, and the PMMA replica was imaged using a spectral-domain OCT (SDOCT) as well as LSCM. The dimensional values from SDOCT and LSCM fluorescence microscopy were compared with each other in order to assess the difference between SDOCT measurements when compared to an established LSCM method. Note that, for this study, the channel structures are within the working distance of the microscope objective used for LSCM imaging, enabling this comparative analysis. In general, LSCM imaging would not be possible when the subsurface channel structures are located a millimetre away from the sample surface, beyond the working distance of the objective lens of LSCM microscopy which are a few hundred micrometres at the most for lenses with a relatively high numerical aperture value. For channels more than the working distance of available objective lenses, cross-sections of an epoxy-filled channel can be imaged by microscopy. This technique is described in the Experimental section.

Experimental

PMMA device

The PMMA device used was obtained from microfluidic ChipShop GmbH, Jena, Germany. The device has a 150 μm thick lid covered on top of four identical linear channels, and the nominal dimensions of the channel cross-section, 50 μm $\times$ 50 μm was provided by the manufacturer. The device was imaged using light and fluorescence microscopy by either filling the channel with a low-viscosity epoxy mixed with a dye or by filling the channel with a fluorophore (Dronpa) in the case of LSCM fluorescence. In the case of the SDOCT, the channel was imaged empty, as it came from the manufacturer.

OCT image acquisition

The sample was imaged with an SDOCT system, as previously described (Chang *et al.*, 2012). Briefly, the SDOCT system (Bioptigen, Raleigh, NC)[1] operated at a centre wavelength of 840 nm with 93 nm full-width at the half-maximum bandwidths, yielding an approximate full-width at the half-maximum coherence length of approximately 3 μm. OCT scans were captured from each sample with 194 B-scans at 1000 A-scans per B-scan. An A-scan obtained with a 4096-array detector is a one-dimensional measure of intensity as a function of distance and a B-scan is a collection of A-scans resulting in an xz image. The B-scans of each data set (xz images) were analyzed using an in-house written ImageJ macro (see below for detailed information). After the analysis of each data set, a table was generated with the number of pixels for the heights and widths of each xz image in the set.

LSCM image acquisition

Axial measurements of the microchannels were obtained by taking xz cross-sectional scans with a laser-scanning confocal Leica TCS SP5 microscope (Leica Microsystems, IL using a 20x/0.7 NA HCX-PL APO objective; Harmonic Compound System – Flat Field and Apochromatic correction objective). The images from each scan were analyzed using an in-house written ImageJ macro (different from the one used for OCT images). The calculated lateral and axial resolution of the LSCM are diffraction-limited, $\approx$ 320 nm and $\approx$ 2.2 μm, respectively (Cole *et al.*, 2011).

Image analysis protocol to determine channel dimensions from the OCT and LSCM images

All image analyses were performed using combinations of standard algorithms in ImageJ (http://rsb.info.nih.gov/ij/). To begin the analysis, a separate region of interest (ROI) which includes the channel cross-section is manually selected for either the OCT or LSCM image series. The ROI is selected such that the entire cross-section of the channel is within the ROI throughout either image series. We tested this method with several different ROIs and found that the results were relatively insensitive to the location and size of the ROI. For both the OCT and the LSCM images, the ROI is then converted to an 8-bit grey scale image and convolved with a median filter with a 5-pixel radius to reduce the random pixel noise in each image.

For the OCT images, the ImageJ "Default" autothreshold was applied to segment the upper and lower surfaces of the channel. After thresholding, the channel height was determined as the vertical distance between the centre of mass of the lower object and the centre of mass of the upper object. The centre of mass was computed as the brightness-weighted average of the x and y coordinates of all pixels in the object. The dimensions of the channel bottom and top were determined from the widths of the bounding box around the thresholded lower and upper objects, respectively.

For the fluorescence LSCM images of the dye-filled channels, the ImageJ "Default" autothreshold was applied to the image, and the channel area was determined directly from the pixels with the intensity above the threshold. The channel dimensions were determined by first generating a binary mask image from the applied autothreshold. One hole filling operation and one erosion operation were executed sequentially on the mask image to remove stray pixels near the edge of the channel that were above the threshold and to preserve the edge contour of the channel. These operations resulted in single, solid object in the mask image. The channel height and the width of the upper surface of the channel were determined from the height and width of the bounding box surrounding the object, respectively. The width of the bottom surface was determined as the width of the bounding box surrounding the lower 15 pixels ($\approx$4 μm) of the channel. A schematic describing the procedure for obtaining these measurements is provided in Figure S1. This was approximately where the channel sidewalls became distinguishable in the image.

Acquisition of cross-section images by bright field and fluorescence microscopy

A low-viscosity epoxy, EP5347 (Eager Polymers, Chicago, IL), was mixed according to the manufacturers specifications. In our case, we mixed 3 g of the A component and 0.6 g of the B component. Then, 4 μL of the fluorescent dye Cell Mask Orange (Invitrogen, Grand Island, NY) was added to the epoxy and mixed again to obtain a uniform distribution of the dye throughout the epoxy. The epoxy/dye mixture was then introduced in the channel through the inlet and aspiration (house vacuum) from the opposite side (outlet) produced the movement and filling of the channel with the epoxy throughout the entire channel. The epoxy/dye was allowed to cure for at least 2 h.

To obtain cross-section images of the channel, a microtome (Leica, Buffalo Grove, IL) was used. Bright field and fluorescence images were collected using an Axioplan 2 with a 40x/0.75 NA objective and an AxioVert 200 with a 40x/0.6 NA objective (Carl Zeiss Microscopes, Thornwood, NY), respectively.

Results and discussion

Determining channel structures from OCT images

The procedure for acquiring OCT images from the lab-on-chip channel is illustrated in Figure 1. Theoretically, the axial

[1] Certain commercial equipment, instruments, or materials are identified in this paper to foster understanding. Such identification does not imply recommendation or endorsement by the National Institute of Standards and Technology, nor does it imply that the materials or equipment are necessarily the best available for the purpose.

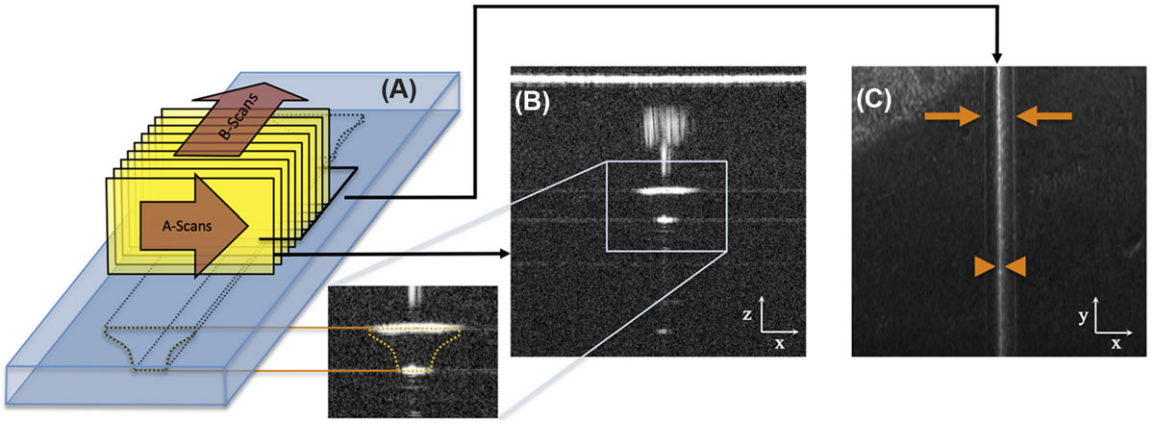

Fig. 1. Scheme of the OCT imaging process. (A) A PMMA lab-on-a-chip device is imaged by scanning the xz plane to obtain a cross-section image of the internal structures. (B) The channel's internal structures are observed in this xz image. The top and bottom sides of the channel are highlighted in the enlarged image coming from the image in B. The sidewalls, which were not apparent in the OCT images, are also delineated to provide an approximation of the area of the channel shown in the cross-section. Arrows represent the direction in z and x and also are scale bars. The scale bar of z represents 100 μm and the scale bar of x represents 150 μm. (C) When the series of xz images is completed, the images are compiled so that the volume of the sample is reconstructed. This image is a top view of the PMMA device and the channel within after reconstruction. The arrows at the top of the image point at the edges delineating the width of the top side of the channel, whereas the arrow heads at the bottom of the image point at the bottom side of the channel (the scale bars have the same dimensions as in B).

resolution, R_{OCT}, for the OCT imaging system is given by the following equation:

$$R_{OCT} = \frac{l_c}{2} \approx 0.44 \frac{\lambda_0}{\Delta\lambda}$$

where l_c represents the coherence length, λ_0 is the source centre wavelength and $\Delta\lambda$ is the source bandwidth. Thus, the SDOCT system operated at a centre wavelength of 840 nm with 93 nm full-width at the half-maximum spectral bandwidth has a theoretical axial resolution of ≈ 3.3 μm (Tomlins *et al.*, 2009). The lateral resolution of OCT is determined by the numerical aperture of the sampling lens (Ding *et al.*, 2002). However, there is a trade-off between the lateral resolution and the focusing depth when conventional lenses are used. Overall, the commercial systems can achieve lateral resolutions of approximately 10 μm or below. The lateral resolution of our SDOCT was estimated from an AFM standard sample fabricated by a UV-masked photolithography sample and was found to be <10 μm.

OCT images of the PMMA lab-on-a-chip device were acquired with the OCT system configuration operating in the spectral domain. Figure 2 illustrates an example of an xz image and the steps followed to process and extract the data from the images. The internal microchannel surfaces (top and bottom sides of the channel), which are embedded in the sealed device, are observed in Figure 2(A). The height and width can be extracted after defining the ROI indicated by the square drawn around the top and bottom lines. Figure 2(B) shows the raw intensity image from the ROI. Figure 2(C) illustrates the image result after applying a median filter with a 5-pixel radius. After completing the processing of the images, the intensities that were above the autothreshold were drawn over the image (Fig. 2D, red areas). From those areas, the height and width of the channel can be obtained and further averages from all xz plane images can be calculated. Notice that the sidewalls of the channel cannot be observed in the SDOCT images. We believe this is primarily due to limited collection efficiency of the backscattered light, which reflects at an angle that is beyond the collection angle of the low numerical aperture SDOCT lens. An attempt to image the sidewall in a tilted sample was not successful as the steep tilted angle does not allow locating the side wall within the focal distance of the SDOCT lens. With this limitation, our SDOCT dimensional analysis is based on the approximation that the average of the top and bottom widths could provide us with the information needed to decide if the channels comply with the expected cross-sectional area. Assuming that the channel shape is trapezoidal, the channel cross-section area is calculated by multiplying the average of both widths times the height [area $= (\text{width}_{\text{top}} + \text{width}_{\text{bottom}})/2) \times$ height)]. The area of a channel could be used as a dimensional parameter to normalize the height and width of channels of different shapes (e.g. trapezoidal vs. square). Therefore, in this work we considered the variability in the area of the channels as a critical parameter.

Determining channel structures from LSCM fluorescence images

To accurately determine the channel dimensions, the lab-on-a-chip device was filled with Dronpa fluorescent dye and imaged using LSCM. The images were analyzed to determine the channel dimensions from each x-z image (Fig. 3). The dimensions are sensitive to the threshold used to process the images.

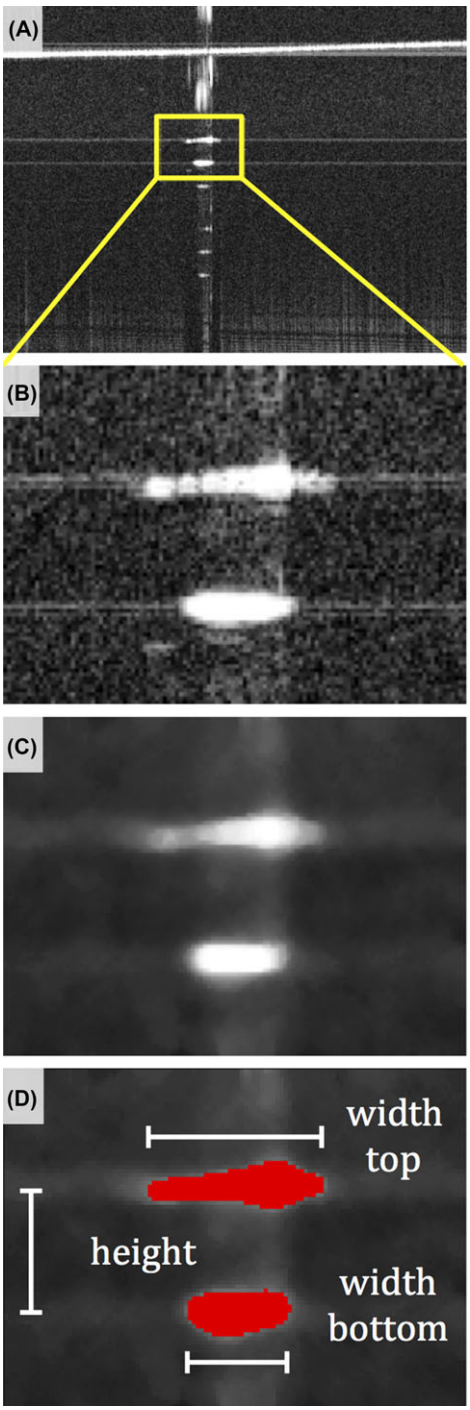

Fig. 2. Determination of the lab-on-a-chip device dimensions from an OCT A-scan slice. (A) The full field of view of a single A-scan slice with a representative region of interest (ROI) indicated with the yellow box. (B) The raw intensity data of the ROI. (C) The ROI in (A) after applying a median filter with a 5-pixel radius. (D) Intensities above the autothreshold are shown in red. The channel height was determined as the vertical distance between the centre of mass of the thresholded bottom region and the centre of mass of the thresholded top region. The width of the channel bottom and width of the channel top were determined from the maximum width of the bottom region and top region, respectively.

The appropriate threshold was determined from regions of the image where the transition from the fluorescence signal to background intensity is largest as described in Figure 3 and in the following text. Several image-processing steps were applied to determine the location of the channel edges. Images were first median-smoothed to remove shot-noise in the photon detection. The smoothed images were then filtered with a Sobel edge detector, and the regions with the largest gradient magnitude were selected using the ImageJ "Default" autothreshold. For the representative image shown in Figure 3, the mean intensity of these pixels computed from the raw intensity image was 92.3 arbitrary units (AU).

To illustrate the range of raw image intensities that correspond to edge regions, line scans across the channel are plotted in Figure 3(D) for the raw, smoothed and gradient images. The gradient maximum (blue line) corresponds to image intensities in the range of 80 to 100 AU. Both these analyses are consistent and suggest that a threshold of 92 AU is appropriate, corresponding to a channel area of 2085 μm^2. For an automated thresholding approach to rapidly detect the channel edges in the large number of images acquired in this study, we applied a method based on the Ridler-Calvard technique (the "Default" autothreshold in ImageJ). The threshold value that results is 86 for the representative image in Figure 4, which corresponds to a channel area of 2138 μm^2 (Ridler and Calvard 1978). The estimated channel area is least sensitive to changes in the intensity thresholds from 80 and 130 (Fig. 3E, red line). In this range, the estimated channel area changes by approximately 9 μm^2 for each unit change in the intensity threshold. Both our analysis of the image gradients and the automated thresholding approach provide similar thresholds that are in the range where the dimensional measurements are least sensitive to changes in the threshold. Therefore, the automated thresholding approach was applied to the entire set of LSCM images and used to compute the channel dimensions for comparison with SDOCT.

Imaging internal device structures by confocal reflectance and interferometric microscopy

Besides SDOCT, attempts were made with two other optical techniques, confocal reflectance microscopy and interferometric microscopy, to image the internal structures of a lab-on-a-chip device. These two modalities were chosen to assess their use for label-free imaging of the device structures. Figure 4 illustrates an xz (cross-sectional) scan of a confocal reflectance image (A) and an LSCM image (B) of a PMMA device with internal structural dimensions reported by the manufacturer of 50 μm $\times$ 50 μm (height and width). A transmission image of the same area is shown in Figure 4(C), and a merged image of all three images is shown in Figure 4(D). As confocal imaging of a thin sample in a reflectance mode would collect enhanced backscattering intensity at sharply kinked corners, we attempted to define the four corners of the

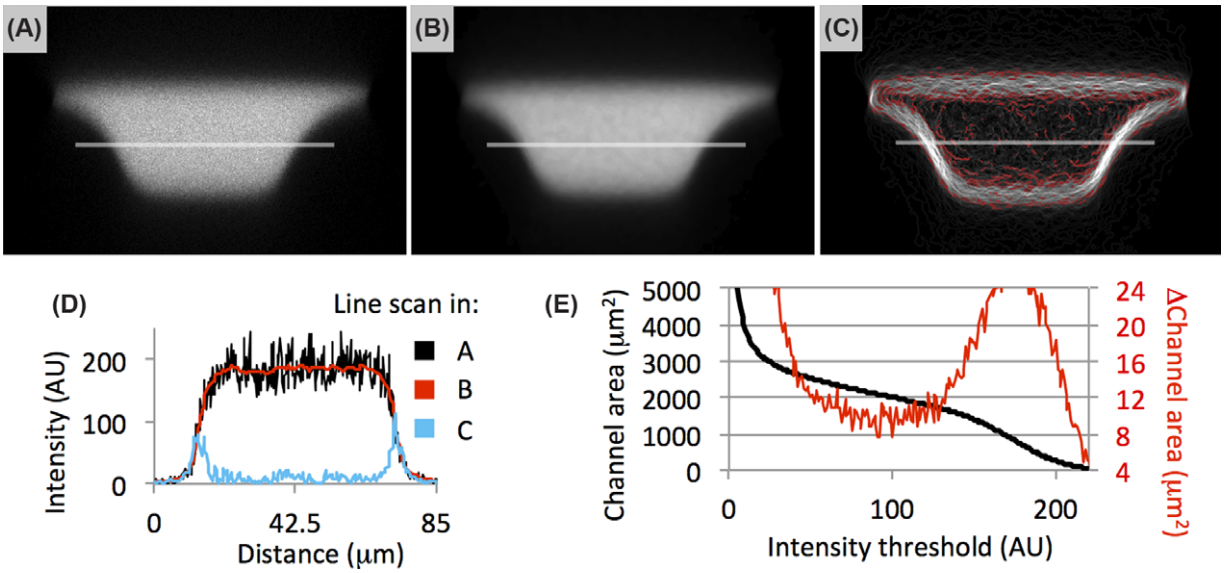

Fig. 3. Estimating the channel dimensions from LSCM fluorescence images of a dye-filled lab on chip device. (A) A representative x-z LSCM fluorescence image. (B) Image in A after median smoothing using a kernel with a 5-pixel radius. (C) Gradient image derived from A after median smoothing followed by filtering with a Sobel edge detector (3 × 3). The regions with the largest gradient magnitude appear as bright pixels and are outlined with red. (D) Plot of intensity as a function of distance for the 1-pixel width line shown in A, B and C for the raw image data (black), after smoothing (red) and after applying the edge detector (blue). The line scan length is 85 μm for each image shown in A, B and C. (E) The area of channel determined as a function of the intensity threshold (dashed black line) and derivative of the area (red line) as a function of the intensity threshold.

channel cross-section from this reflectance mode image. However, the confocal reflectance image indicates interference of the coherent laser beam reflecting off multiple interfacial layers. This artefact distorts the image of the top and bottom channel surfaces and makes automated analysis challenging. For this reason, confocal reflectance imaging was not considered further. In comparison, the LSCM fluorescence image is less ambiguous, showing the shape of the channel and providing a more direct measurement of the channel dimensions.

Another technique that could be used for this purpose is interferometry microscopy. However, attempts to image the internal structures of this device using interferometric microscopy were intractable and therefore no comparisons were possible with that technique. We believe that the failure to achieve interpretable results on the PMMA devices arises from the lack of complete transparency of this material in the visible range.

Comparison of SDOCT and LSCM dimensional measurements

We compared the SDOCT and the LSCM dimensional measurements by analysing 290 xz cross-sectional plane images from each technique acquired from the same lab-on-a-chip device. Measurements were taken from three regions of a PMMA channel with nominal cross-sectional dimensions of 50 μm × 50 μm provided by the manufacturer. The channel width at top, width at bottom and height were calculated for each technique as described in the Methods and the results are plotted in Figures 5(A–C). All dimensional measurements are reported as the mean ± SD.

The values obtained for the width at the top of the channel (Fig. 5A) show that there is not a statistically significant difference between the two techniques. The widths at top obtained with LSCM and SDOCT were 76.0 ± 0.8 μm and 75 ± 12 μm, respectively. The measurement with LSCM was highly consistent within replicates and between different regions (CV = 1%, n = 290; CV = 1%, n = 3, respectively). On the other hand, the measurements with SDOCT had a much greater dispersion both within each region's replicates (CV = 16%, n = 290) and among the different regions (CV = 8.7%, n = 3). The larger dispersion for the SDOCT-based measurement likely results from the poor lateral resolution of the technique (<10 μm) and the poor image contrast present at the interface between the lid and the chip. Both these factors resulted in the width of the thresholded region (see Fig. 2) varying from image to image. Comparatively, the LSCM image is less ambiguous for determining the width at the top.

We observed a statistically significant difference between the LSCM and SDOCT measurements for the width at the bottom of the channel (40 ± 2 μm for LSCM and 30 ± 4 μm for SDOCT). One possibility for the discrepancy between the two techniques is that the curvature at the edges of the bottom surface provides low contrast in SDOCT and is not accurately detected. This low contrast SDOCT at the bottom edge is attributed to relatively sharp corner resulting in vertically steep inner wall from which the collection of reflecting backscattering signal

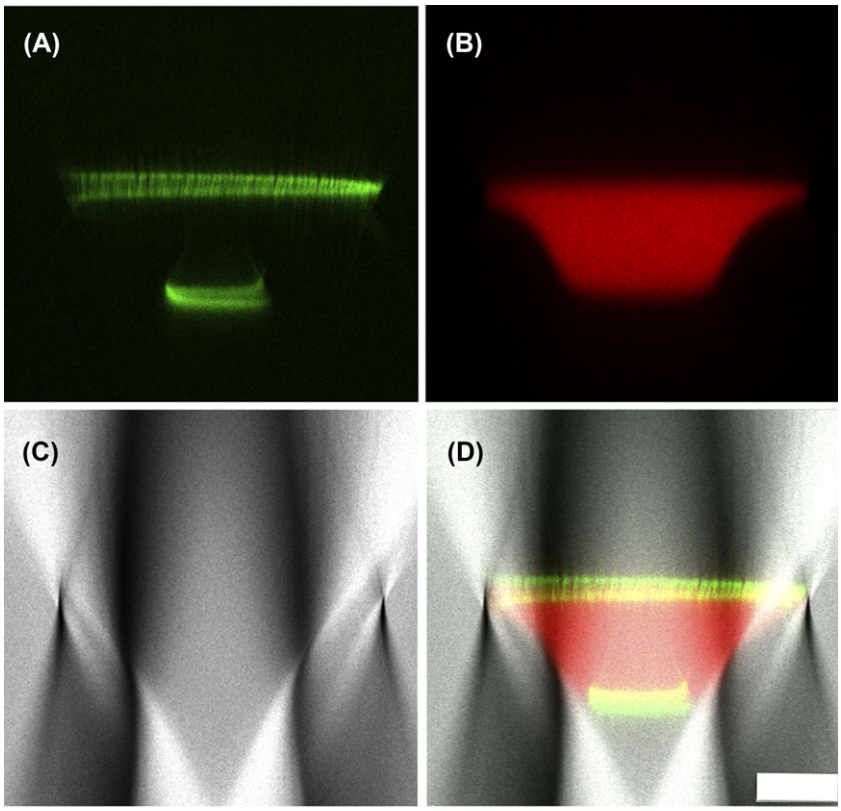

Fig. 4. LSCM images of a PMMA-molded channel (50 μm high and 50 μm wide, as stated by the manufacturer) covered with a PMMA thin film (approximately 250 μm thick). (A) Confocal reflectance (backscattering) micrograph of the channel shows the top and bottom sides of the channel from which the width and height of the channel can be obtained. (B) LSCM fluorescence micrograph obtained by filling the channel with a solution of Dronpa. The channel conformation can be seen with this imaging mode. However, it is more difficult than in the previous image to determine the end of physical (dimensional) limits of the channel. (C) Transmission micrograph of the same channel area as in A and B. Note that dimensional information from this image is difficult to obtained due to scattering occurring in the channel. (D) A merged image of A, B and C. The combination of the three micrographs provides a better idea of the dimensional features of the channel. Scale bar (lateral and axial): 25 μm.

is substantially diminished. This structural detail is confirmed from the cross-sectional images of a microtomed epoxy-filled channel described later. Quantification of the structural details may be possible by analyzing a series of these cross-section samples. The measurement of the width at the bottom by LSCM (Fig. 5B) was consistent within replicates (CV = 6%, $n = 290$) and highly consistent between different regions (CV = 2%, $n = 3$). The SDOCT measurements had a much greater dispersion for both the replicates within each region (CV = 14%, $n = 290$), and between the different regions (CV = 15%, $n = 3$). The larger dispersion for the SDOCT-based measurement can be explained similarly to the large dispersion for the width at the top measurement. Because of the poor lateral resolution of SDOCT, the width of the thresholded region varies from image to image (Fig. 2). Additionally, the curvature at the bottom can result in SDOCT contrast that diminishes gradually over a large (lateral) length scale and can be a source of additional variability in the width of the thresholded region.

We observed a statistically significant difference between the LSCM and SDOCT measurements for the height of the channel (Fig. 5C). Specifically, the values obtained for the height were 43 $\pm$ 2 μm and 49 $\pm$ 2 μm for the LSCM and SDOCT, respectively. The reason for SDOCT providing a 6 μm larger height compared to LSCM is not clear, but highlights the challenge for measuring internal structures of lab-on-a-chip devices. The height measurements obtained by both techniques were highly consistent within replicates (CV = 4% in both cases, $n = 290$), as well as between different regions (CV = 1% for both techniques, $n = 3$). The high precision and repeatability of both techniques is indicated by the low CV for the replicate measurements. Despite the LSCM having a significantly lower axial resolution compared to OCT (0.32 vs. 3.3 μm, respectively; see supporting information), the precision of both techniques can be attributed to similar underlying optical principles. In the case of the LSCM, our image analysis procedure finds the midpoint of the intensity gradient between the channel and the background fluorescence. The gradient occurs because of the point spread function of the imaging system and limits our ability to determine the true width of the edge accurately. However, we can determine the location

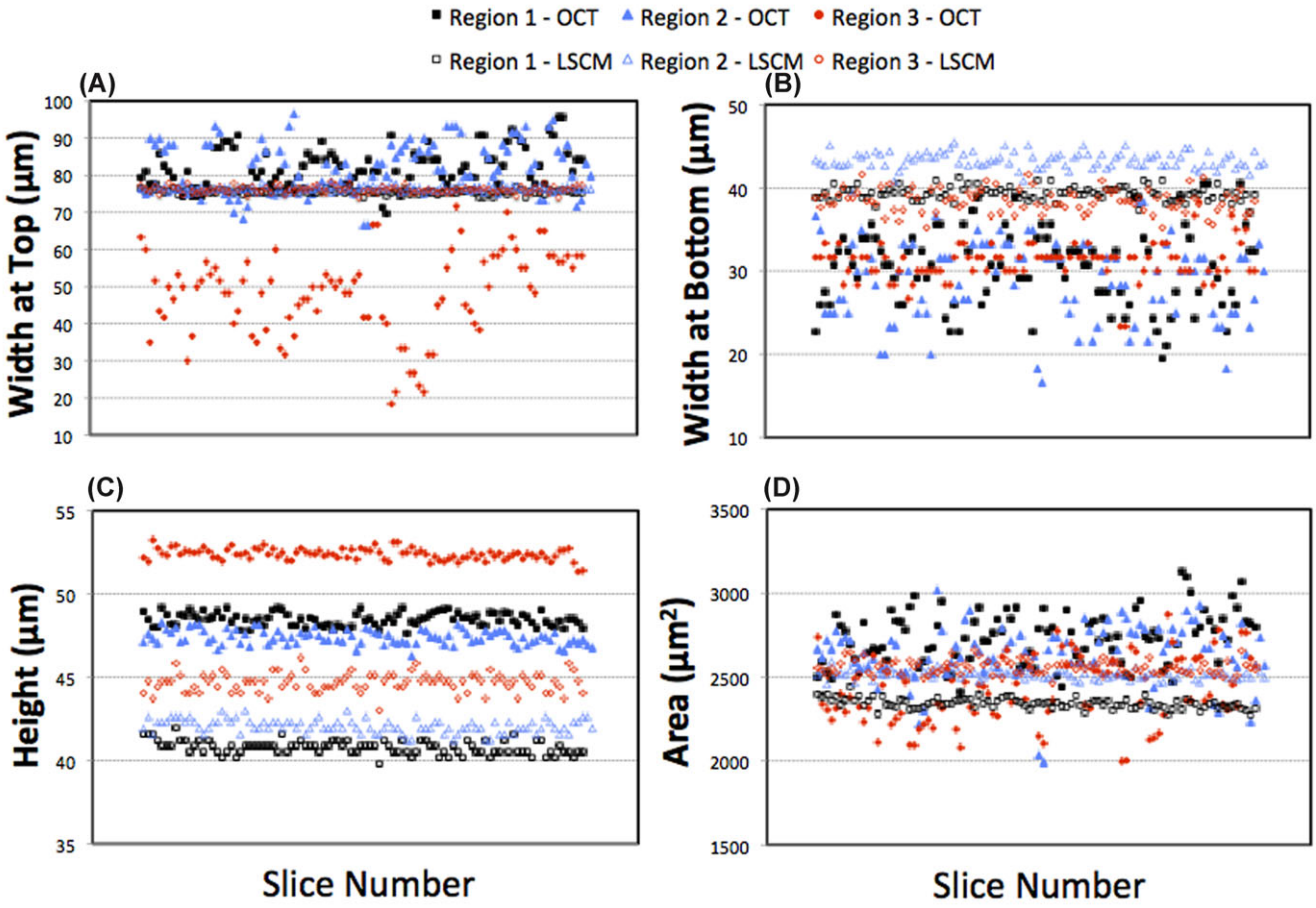

Fig. 5. Plot of the values obtained for each measurement of the width at top (A), width at bottom (B), height (C) and for the calculated area (D) for the three regions measured in a 50 μm × 50 μm channel.

of the top and bottom edges with high accuracy at the centres of the intensity gradients. Similarly, the location of the top and bottom surfaces of the channel can be determined with high accuracy in SDOCT by finding the centroid of the top and bottom channel surfaces.

The values obtained for the calculated area showed a statistically significant difference between the LSCM and SDOCT (Fig. 5D). The calculated values for the areas were 2474 ± 100 μm and 2599 ± 222 μm for LSCM and SDOCT, respectively. The estimated channel area by SDOCT is 5% larger compared to LSCM. The area obtained with LSCM was highly consistent within replicates (CV = 4%, $n = 290$) and between different regions (CV = 2%, $n = 3$). The SDOCT measurements had a greater dispersion for both the replicates within each region (CV = 9%, $n = 290$), and between the different regions (CV = 9%, $n = 3$). This is likely due to the variability in both width measurements because the height was highly consistent.

One of the parameters considered in the lab-on-a-chip field as critical is the backpressure produced by existing features before and after the functional element within the microchannel network (Becker, 2010). In our case, the dimensional parameters of the channel are the features of interest in our device, which will generate a higher or lower resistance than expected depending upon the actual dimensions of the system. If we were to compare the expected nominal area of 2500 μm^2 (50 μm × 50 μm), the difference in area from this expected value would be 1% and 4% for LSCM and SDOCT, respectively. However, the actual area of the device is not really known. We believe the best estimate of the dimensions of the channel is obtained by cross-sectioning of the channel with a microtome and imaging with a calibrated microscope and measuring the dimensions of the cross-section.

Internal device measurements using cross-sectional microimaging

A cross-sectional image was acquired after all other measurements (LSCM and SDOCT) were obtained and the results analyzed to avoid any biases in the treatment of the LSCM and OCT data. Cross-section images of a region in the channel in which dimensions were measured using SDOCT and LSCM (Region 1) were obtained (Fig. 6). To preserve as much as possible the shape of the channel during the microtoming

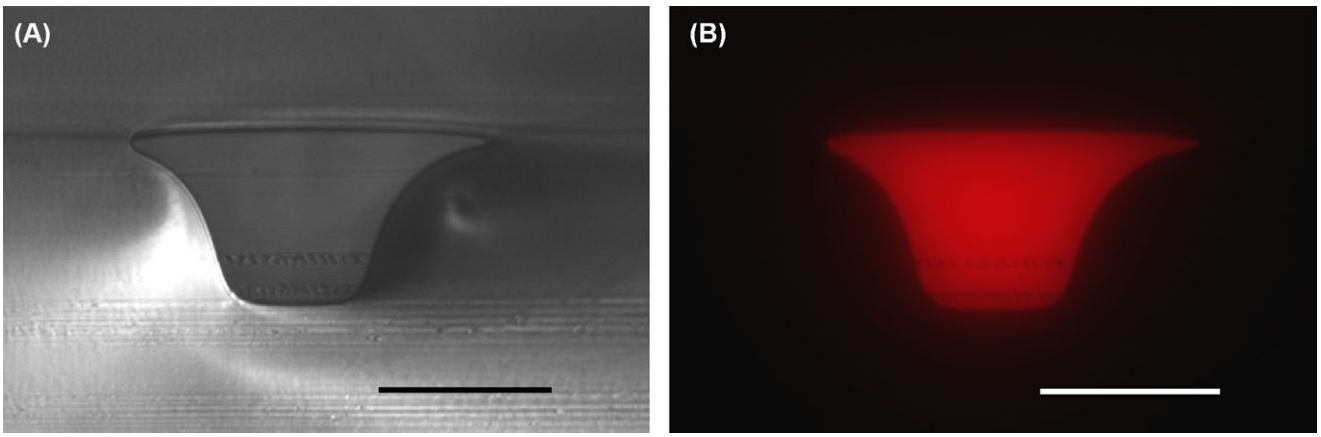

Fig. 6. Micrographs of a cross-section of Region 1 of the channel, from which SDOCT and LSCM measurements were obtained. (A) Bright field image of the channel filled with a mixture of epoxy and fluorescent dye. (B) Fluorescence image of the same surface as in A. The shape and dimensions measured with both microscopes are similar (≤1%). The size of scale bars is 50 μm.

Table 1. Comparison of values obtained for the Region 1 of a channel dimensions measured by bright field and fluorescence microscopies, LSCM and OCT.

Dimensions	Cross-section[a]	LSCM	OCT	% Dev. LSCM	% Dev. OCT
Height (μm)	50.9 (BF)	40.8 ± 0.4	48.5 ± 0.4	20*	4.7*
	50.6 (Fl)			19$^{\vee}$	4.2$^{\vee}$
Width at top (μm)	104 (BF)	75 ± 1	82 ± 5	28*	21*
	104 (Fl)			28$^{\vee}$	21$^{\vee}$
Width at bottom (μm)	36.7 (BF)	39 ± 1	31 ± 5	6*	16*
	37.2 (Fl)			5$^{\vee}$	17$^{\vee}$
Average width (μm)	70.3 (BF)	57 ± 1	56 ± 3	19*	20*
	70.8 (Fl)			19$^{\vee}$	21$^{\vee}$
Area from ImageJ (μm^2)[b]	3068 (BF)	2326 ± 47	2716 ± 147	24*	11*
	3025 (Fl)			23$^{\vee}$	10$^{\vee}$
Calculated Area (μm^2)[c]	3579 (BF)	2326 ± 47	2716 ± 147	35*	24*
	3581 (Fl)			35$^{\vee}$	24$^{\vee}$

[a] Average of the measurements done with bright field and fluorescence microscopies.
[b] Apply only to the cross-section images. The limits of the two images were delineated using ImageJ and the area calculated based on the conversion of pixels to micrometres.
[c] Obtained from the product of the average of the top and bottom width and the height.
* Compared to BF; $^{\vee}$ compared to Fl.
BF, bright field; Fl, fluorescence.

process, we filled the channel with a mixture of epoxy/dye. The epoxy/dye inside the channel allowed for imaging by bright field and fluorescence (Figs. 6A, B, respectively). Both images are consistent, although taken in different microscopes, the relative errors of the two measurements combined were <1% in all cases. It is worth noting that the images in Figure 6 show the trapezoidal shape observed in Figure 4(B), using LSCM. However, the edges surrounding the channel are better defined providing a less ambiguous determination of the dimensions of the channel.

Table 1 shows the results for all the Region 1 measurements, and the percentage deviation obtained from the cross-section measurements (taken here as the reference measurement) in comparison with the LSCM and SDOCT. In order to obtain the dimensional values of the cross-section images tangents were drawn parallel to the sidewalls of the channel. A line parallel to the base of the channel was drawn and where this intersected with the tangents was determined to be the corners of the channel. From those lines drawn the height, and width at top and width at bottom of the channel cross-sections were obtained. From all the dimensional measurements taken, when comparing with our reference measurement (cross-section), the height obtained with SDOCT was the closest with a difference of about 4%.

The dimensional measurements that followed were the width at the bottom, using LSCM, with a difference between

5% and 6%. Then the area, when compared with the area obtained with the cross-section using ImageJ, differed by 10% to 11%. Overall, SDOCT showed lower differences for the height, width at the top, and the calculated area as well as the area obtained using ImageJ. On the other hand, the LSCM measurements produced a lower difference for the width at bottom. The differences obtained for the average width with LSCM and SDOCT were similar (19% and 21%, respectively). We believe the larger differences obtained between the cross-section images and the LSCM images are most likely due to the dimmer fluorescence emitted from the back and far end of the channel, producing a smaller dimensional value than the real one.

Conclusions

In this work, we demonstrate the use of LSCM and SDOCT to determine the dimensions of microfluidic channels made of PMMA and, to some extent, the capabilities of both techniques in obtaining the "true" dimensional values for this type of sample. The variability of the results obtained with these techniques highlights the difficulties when attempting to unambiguously determine the dimensional values of critical parameters including channel width, height and cross-sectional area, in microfluidic final products.

In general, SDOCT showed more accurate height measurements than LSCM. On the other hand, LSCM produced better shape representation, but less accurate height measurements. Different techniques often produce different dimensional results due to the limitations and biases each technique presents. Ultimately, a solution to this challenge will likely come from a combination of techniques that could simultaneously measure the dimensions of microfluidic critical parameters taking advantage of the strengths each technique used may provide.

Acknowledgements

This project was funded internally by the National Institute of Standards and Technology (NIST). We would like to thank Dr. Steven Hudson for his help in cutting the PMMA microfluidic channels to obtain cross-sections for imaging.

References

Becker, H. (2010) One size fits all? *Lab. Chip.* **10**, 1894–1897.

Beebe, D.J., Mensing G.A. & Walker G.M. (2002) Physics and applications of microfluidics in biology. *Annu. Rev. Biomed. Eng.* **4**, 261–286.

Chang, R.C., Johnson, P., Stafford, C.M. & Hwang, J. (2012) Fabrication and characterization of a multilayered optical tissue model with embedded scattering microspheres in polymeric materials. *Biomed. Opt. Express.* **3**, 1326–1339.

Choma, M.A., Sarunic, M.V., Yang, C.H. & Izatt, J.A. (2003) Sensitivity advantage of swept source and Fourier domain optical coherence tomography. *Opt. Express.* **11**, 2183–2189.

Cole, R.W., Jinadasa, T. & Brown C.M. (2011) Measuring and interpreting point spread functions to determine confocal microscope resolution and ensure quality control. *Nat. Protoc.* **6**, 1929–1941.

de Boer, J.F., Cense, B., Park, B.H., Pierce, M.C., Tearney, G.J. & Bouma, B.E. (2003) Improved signal-to-noise ratio in spectral-domain compared with time-domain optical coherence tomography. *Opt. Lett.*, **28**, 2067–2069.

Ding, Z.H., Ren, H.W., Zhao, Y.H., Nelson, J.S. & Chen, Z.P. (2002) High-resolution optical coherence tomography over a large depth range with an axicon lens. *Opt. Lett.*, **27**, 243–245.

Drexler, W. & Fujimoto, J.G. (2008) State-of-the-art retinal optical coherence tomography. *Prog. Retin. Eye Res.* **27**, 45–88.

Frohman, E.M., Fujimoto, J.G., Frohman, T.C., Calabresi, P.A., Cutter, G. & Balcer, L.J. (2008) Optical coherence tomography: a window into the mechanisms of multiple sclerosis. *Nat. Clin. Pract. Neuro.* **4**, 664–675.

Leitgeb, R., Hitzenberger, C.K. & Fercher, A.F. (2003) Performance of Fourier domain vs. time domain optical coherence tomography. *Opt. Express.* **11**, 889–894.

Li, S., Xu, Z., Yoon, S.F. & Fang, Z.P. (2011) Feasibility study on bonding quality inspection of microfluidic devices by optical coherence tomography. *J. Biomed. Opt.* **16**, 066011-1–066011-9.

Ridler, T.W. & Calvard, S. (1978) Picture thresholding using an iterative selection method. *IEEE Trans. Syst. Man Cybern.* **8**, 630–632.

Stavis, S. (2012) A glowing future for lab on a chip testing standards. *Lab. Chip.* **12**, 3008–3011.

Tomlins, P.H., Ferguson, R.A., Hart, C. & Woolliams, P.D. (2009) Point-Spread Function Phantoms for Optical Coherence Tomography. National Physical Laboratory (NPL) Report OP 2, pp 2–4.

Villey, R., Carrion, L., Morneau, D., Boudoux, C. & Maciejko, R. (2010) High-velocity-flow imaging with real-time Doppler optical coherent tomography. *Appl. Opt.* **49**, 3140–3149.

Supporting Information

Additional Supporting information may be found in the online version of this article at the publisher's website:

Fig. S1. Schematic representation of the image analysis procedure to determine the channel width at top, width at bottom and height from LSCM images. (A) Representative LSCM image (Fig. 3A). (B) After applying threshold, pixels above the threshold shown in red. The bounding box around the channel is shown (white), from which the width at top and height are determined. The bounding box surrounding the lower 15 pixels ($\approx 4\ \mu$m) of the channel is shown (yellow), from which the width at bottom was determined.